Hindawi
International Journal of Energy Research
Volume 2023, Article ID 4176447, 14 pages
https://doi.org/10.1155/2023/4176447

Research Article

Sulfur-Rich N-Doped Co_9S_8 Catalyst for Highly Efficient and Durable Overall Water Electrolysis Application

Abu Talha Aqueel Ahmed,[1] **Jonghoon Han**,[1] **Giho Shin**,[1] **Sunjung Park**,[1] **Seungun Yeon**,[1] **Youngsin Park**,[2] **Hyungsang Kim**,[1] **and Hyunsik Im**[1]

[1]*Division of Physics and Semiconductor Science, Dongguk University, Seoul 04620, Republic of Korea*
[2]*Department of Chemistry, College of Natural Science, Ulsan National Institute of Science and Technology (UNIST), Ulsan 44919, Republic of Korea*

Correspondence should be addressed to Hyungsang Kim; hskim@dongguk.edu and Hyunsik Im; hyunsik7@dongguk.edu

Received 10 September 2022; Revised 31 October 2022; Accepted 3 November 2022; Published 7 February 2023

Academic Editor: Kisan Chhetri

Facile template–free controllable growth of freestanding polyhedron–like CoS onto microporous Ni foam with three-dimensional architecture via a mild hydrothermal technique is reported. The as-obtained CoS catalyst phase was first tailored to N-Co_9S_8 (nitrogen doped Co_9S_8), and its inherent reaction kinetics and conductivity were then enhanced through sulfur incorporation via a hydrothermal process. The electrochemical performance of the pristine CoS and a sulfur-enriched N-Co_9S_8 (S, N-Co_9S_8) electrode in alkaline 1.0 M KOH was examined. The optimized polyhedral S, N-Co_9S_8 structured catalyst exhibits significantly enhanced electrocatalytic activity for both oxygen evolution reaction (OER) and hydrogen evolution reaction (HER). As a result, low overpotentials of 244 and −92 mV is required to achieve the current density of 10 mA cm^{-2} for the OER and HER, respectively. Furthermore, when the polyhedral S, N-Co_9S_8 catalyst was employed as a bifunctional catalyst in a two-electrode electrolyzer cell exhibiting a cell voltage of 1.549 V at 10 mA cm^{-2} and demonstrates excellent long-term (50 hrs.) chronopotentiometric electrolysis at various current rate, reveals excellent bifunctional OER and HER activities at different applied current densities. The superior OER and HER activities of the S, N-Co_9S_8 catalyst is result of the improved electronic conductivity and enhanced intrinsic reaction kinetics, which led to the enhanced electrocatalytically active sites after the incorporation of heteroatoms in the catalyst structure.

1. Introduction

Hydrogen (H_2) is considered an alternative to traditional fossil fuels (e.g., coal, petrol, and natural gas) for various energy applications, and its use could limit greenhouse gas emissions caused by the use of fossil fuels [1–3]. Clean, renewable, and highly efficient H_2 fuel can be easily produced through the sustainable ecofriendly electrochemical water splitting technique [4, 5]. An electrolysis of Earth-abundant water is a promising approach to generate pure oxygen (O_2) and H_2 gases without any carbon emission. These gases are generated by two main half-cell reactions, namely (1) oxygen evolution reaction (OER) and (2) hydrogen evolution reaction (HER), respectively. These reactions occur at the anode and cathode, both of which should be made of highly efficient and durable catalyst materials that have a small overpotential (η) in alkaline electrolyte media [6–8]. Although RuO_2/IrO_2- (OER catalyst) and Pt-based (HER catalyst) electrode materials have been considered as highly efficient, stable, active, and reliable. However, their low abundance, high cost, and material scarcity hinder their practicability in mass production [9, 10].

The overall performance of an electrolyzer cell primarily depends on the employed active OER and HER electrocatalyst [11, 12]. To date, various transition-metal-based electrocatalysts have been investigated as individual electrocatalysts for the OER and HER in alkaline and acidic media [13–17]. However, their bifunctionality lags behind than that of the precious-metal-based catalysts due to inefficient kinetics in a single electrolyte medium [3]. For example, due to its high

conductivity, intrinsic kinematics, robustness, mixed valence state, and efficient and durable electrochemical activity, Co_9S_8 is considered a promising electrocatalyst material [13–15], but it suffers from poor electrochemical activity arising from its sluggish kinetics during catalytic OER and HER processes [18–20]. The catalytic activity of an electrocatalyst is mainly determined by its electronic structure, which can be altered intrinsically via the addition of heteroatoms (e.g., N and S) to the host structure [21, 22]. The unfilled outermost 2p and 3p respective orbitals of N and S exhibit promising electron-withdrawing ability and high electronegativity due to the capture of electrons from adjacent Co atoms via acceptor/donor interactions [17, 21, 23]. This can lead to a change in the intrinsic electronic structure of Co_9S_8 and result in the optimal adsorption and dissociation of H_2O molecules on the surface due to the reduced Gibbs's free energy [3, 7]. Moreover, the addition of sulfur to the host structure minimizes the free energy of hydrogen adsorption and weakens the interaction between the anion and the metal on the catalyst surface [12, 23, 24]. Thus, the inclusion of metal heteroatoms with numerous free electrons in the structure of an active catalyst material would be a promising strategy for the improvement of the surface state density, which results in efficient and stable catalytic OER and HER activity [3].

Inspired by the above key consideration, herein, we report the design and synthesis of sulfur-rich nitrogen-doped Co_9S_8 (S, N-Co_9S_8), which can be used as a bifunctional electrocatalyst practically at wide industrial scale, prepared via a hydrothermal experimental procedure followed by nitrogen annealing with subsequent anion-exchange process. At first, a freestanding polyhedral-like CoS catalyst electrode film was prepared through a mild hydrothermal procedure. The structural phase of the pristine catalyst changed from CoS to S, N-Co_9S_8 upon treatment with N_2 and subsequent anion-exchange procedure. The electrochemical performance of all prepared catalysts were then investigated in an alkaline electrolyte medium (1.0 M KOH). Figure 1 shows the experimental schematic and the steps involved for the fabrication of the proposed catalysts. The optimized S, N-Co_9S_8 bifunctional catalyst shows an excellent electrochemical OER and HER activities, achieves the low overpotentials of 244 and −92 mV, respectively, at a current density of 10 mA cm^{-2}. Moreover, this electrocatalyst exhibits an elevated intrinsic activity and higher reaction kinetics compared to as-prepared CoS catalyst. The S, N-Co_9S_8 catalyst exhibits the pretentious electrocatalytic OER and HER performances comparable to other metal-sulfide-based catalysts reported previously in KOH electrolyte medium (summarized in Figure 2(a) and 2(b)) [25–32]. Moreover, the S, N-Co_9S_8 bifunctional catalyst shows a static voltage response at different current rates and superior ultralong stability at a high current rate of 100 mA cm^{-2}.

2. Experimental Section

2.1. Chemical and Materials. The analytical grade chemicals were used in the present work; those were purchased from Sigma Aldrich. Cobalt chloride hexahydrate ($CoCl_2{\cdot}6H_2O$), sodium citrate tribasic dihydrate ($C_6H_5Na_3O_7{\cdot}2H_2O$), thioacetamide ($C_2H_5NS$), thiourea ($CH_4N_2S$), ruthenium oxide ($RuO_2$), commercial 20 wt.% platinum on graphitized carbon (Pt/C), and potassium hydroxide (KOH) pellets were used without any further purification. Three-dimensional (3D) Ni foam (NF, sheet size: 20 × 30 cm, thickness: 1.6 mm, and cell size: 450 μm) was bought from Alantum Corporation (Korea) and used after cleaning with DI water, acetone, ethanol, and HCl several times.

2.2. Fabrication of CoS, N-Co_9S_8, and S, N-Co_9S_8 Catalyst Films. First, a freestanding polyhedral network of CoS was grown on a 3D NF substrate (size: 5 cm × 1 cm; exposed area: 1 cm × 1 cm) via a hydrothermal technique [33]. The active material phase was then transformed into N-doped Co_9S_8 (N-Co_9S_8) via annealing at N_2 ambient. The N-Co_9S_8 was further subjected to anion-exchange process to obtain the S-rich N-Co_9S_8 (S, N-Co_9S_8). In a typical synthesis, an equimolar amount of $CoCl_2{\cdot}6H_2O$ and $C_6H_5Na_3O_7{\cdot}2H_2O$ were dissolved at ambient temperature in a 50 mL aqueous solution of C_2H_5NS (18 mmol) under vigorous stirring for about 30 minutes (min). The mixture solution and precleaned NF substrate were transferred into a 0.1 L Teflon-lined stainless-steel autoclave. The autoclave assembly was placed in a muffle furnace. A hydrothermal experiment was performed for 6 hours (h) at 150°C with a ramping rate of 1°C/min. The CoS electrode film was collected from the autoclave, rinsed numerous times with deionized water and ethanol, and dried in a vacuum ambient. The N-Co_9S_8 and S, N-Co_9S_8 were then prepared from the as-obtained CoS film. The CoS electrode was annealed in a N_2 environment for about 3 h at 700 K to obtain N-Co_9S_8 and subsequently an anion-exchange process was performed for about 10 h at 120°C in a 50 mL solution of 0.1 M CH_4N_2S to get the S, N-Co_9S_8 catalyst electrode [34].

2.3. Fabrication of RuO_2 and Pt/C Catalyst Films. The RuO_2 and Pt/C films were fabricated using a simple drop casting approach. Commercially obtained RuO_2 or Pt/C powder was separately dispersed in 1.00 mL of ethanol containing 0.15 wt.% Nafion. The as-obtained solutions were sonicated for about 1 h, drop-casted on NF (1 cm × 1 cm), and vacuum-dried overnight.

2.4. Characterization Methods. The crystal phase and material structure of the catalyst electrode were investigated using X-ray diffraction (XRD; model: Rigaku Smartlab instrument). The catalyst electrode's morphology and material/chemical composition were determined using field-emission scanning electron microscopy (FE-SEM) and energy-dispersive X-ray spectroscopy (EDS; Model: JSM–6701F) techniques, respectively. The elemental binding states and material chemical fingerprint were analyzed using X-ray photoelectron spectroscopy (XPS; model: ULVAC PHI 5000 VersaProbe) and the Raman spectra analysis techniques (model: LabRam Armis instrument, Horiba Jobin Yvon), respectively. High angle annular dark field (HAADF) scanning transmission electron microscopy (STEM) and

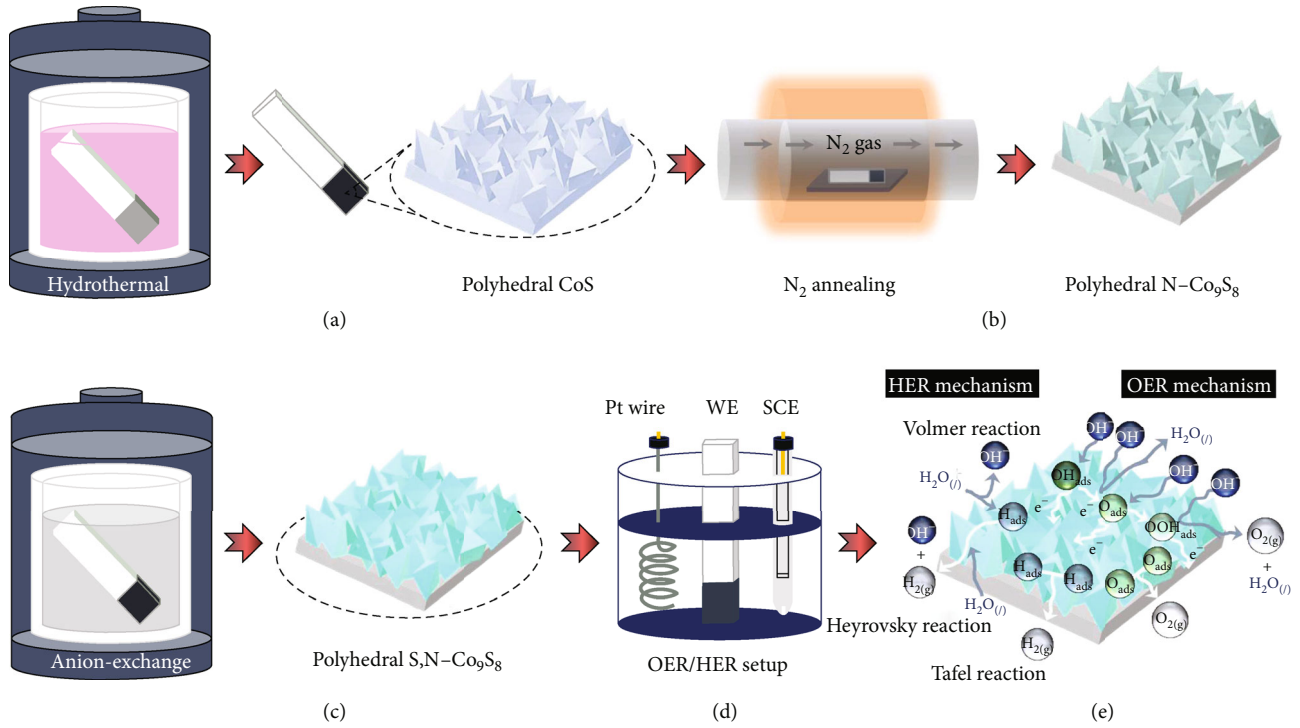

FIGURE 1: Schematic illustration of the experimental process for the fabrication of the CoS, N-Co_9S_8, and S,N-Co_9S_8 catalysts. (a) Autoclave containing the mixed solution and precleaned NF substrate. The CoS phase was obtained at 150°C with a deposition time of 6 h. (b) The proposed S,N-Co_9S_8 catalyst electrode was obtained under an N_2 environment (3 h at 700 K; N-Co_9S_8), and (c) the subsequent anion-exchange process was conducted in 0.1 M CH_4N_2S at 120°C for 10 h. (d) Experimental three-electrode setup for electrocatalytic OER and HER activities. (e) Typical electrocatalytic OER and HER reaction mechanisms in 1.0 M KOH electrolyte.

elemental line scan mapping were carried out using a JEOL-2010 microscope at 200 kV with an X-ray EDS accessory.

2.5. Electrochemical Measurements

2.5.1. Catalyst Electrode Configurations for OER and HER. The electrochemical OER and HER performance of the prepared catalyst electrodes were examined using a conventional three-electrode electrochemical analyzer (VersaSTAT system, Princeton Applied Research) in 1.0 M alkaline KOH electrolyte. The prepared (CoS, N-Co_9S_8, and S, N-Co_9S_8) catalyst electrodes were used as the working electrodes. A platinum wire and a saturated calomel electrode (SCE) were served as the counter and reference electrodes, respectively. Cyclic voltammetry (CV) curves were recorded as a function of the scan rate (v) within a fixed non-Faradaic voltage window range to estimate the electrocatalytically active surface sites/area (ECSA) as follows: [35]

$$\text{ECSA} = \frac{C_{DL}}{C_E}, \qquad C_{DL} = \frac{J_{DL}}{v}, \tag{1}$$

where C_E (0.04 mF for KOH) is the specific capacitance of electrolyte and C_{DL}, J_{DL}, and v are the double-layer capacitance, current density, and scan rate, respectively. Linear sweep voltammetry (LSV, polarization) and a chronopotentiometry test were conducted to analyze the potential response of the catalyst for different current densities. Electrochemical impedance spectroscopy (EIS) was used to understand the charge transfer kinetics of the catalyst electrode material at the electrode/electrolyte interface.

2.5.2. Bifunctional Electrolyzer Configurations. The bifunctional electrocatalytic performance of the optimized S, N-Co_9S_8 catalyst electrode was investigated using an electrochemical analyzer (VersaSTAT instrument) in a two-electrode configuration. The S, N-Co_9S_8 catalyst was served as both the anode and cathode in the electrolyzer cell and all the measurements were conducted in 1.0 KOH electrolyte.

3. Results and Discussion

The material phase and crystal structure of the CoS, N-Co_9S_8, and S, N-Co_9S_8 catalyst electrodes were examined using the XRD technique [36]. Figure 2(c) shows the XRD patterns of the prepared CoS, N-Co_9S_8, and S, N-Co_9S_8 species. The XRD spectrum of each catalyst shows distinct diffraction peaks, indicating that the good crystallinity of the cobalt sulfide phases formed. The diffraction peaks at the bottom (black spectrum) present at 30.89°, 35.76°, 47.43°, 55.00°, and 75.03° can be assigned to the (100), (101), (102), (110), and (202) planes of hexagonal CoS (JCPDS card No. 75-0605), respectively. The diffraction peaks at

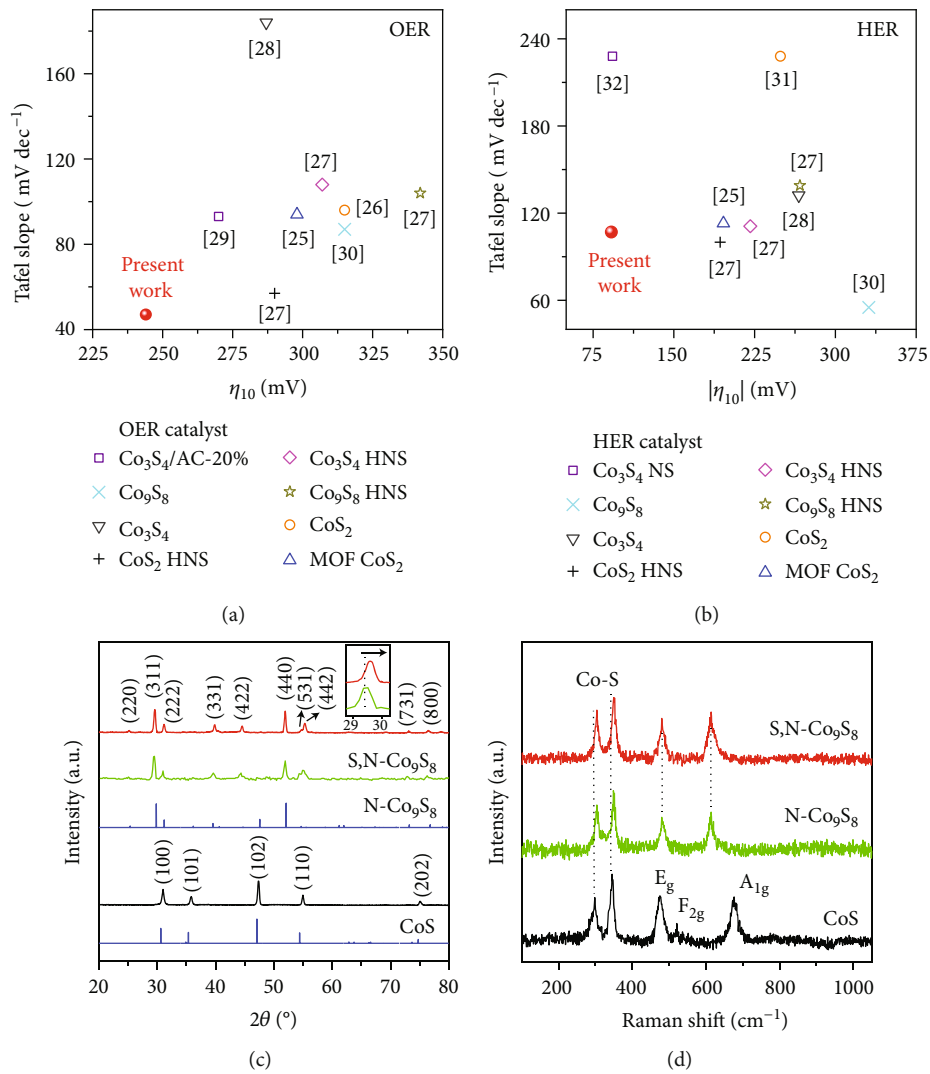

FIGURE 2: Comparative electrocatalytic (a) OER and (b) HER performance of the S,N-Co_9S_8 catalyst with previously reported metal-sulfide-based catalysts measured in a 1.0 M KOH electrolyte medium. The η_{10} represents all of the overpotentials reported at 10 mA cm^{-2}. (c) XRD and (d) Raman spectra for the CoS, N-Co_9S_8, and S,N-Co_9S_8 catalyst electrodes.

the top (green spectrum) located at 25.13°, 29.48°, 31.08°, 39.72°, 44.49°, 51.92°, 54.67°, 55.12°, 73.03°, and 76.36° can be indexed to the (220), (311), (222), (331), (422), (440), (531), (442), (731), and (800) planes of cubic Co_9S_8 (JCPDS card No. 86-2273), respectively. Both the N-Co_9S_8 (green spectrum) and S, N-Co_9S_8 (red spectrum) catalysts reveal similar reflection planes. However, the S, N-Co_9S_8 catalyst shows an apparent positive shift (29.48° to 29.56°) in the diffraction peak corresponding to the reflection of the (311) plane, indicating the successful incorporation of S atoms into the N-Co_9S_8 lattice, which results in a lower interplanar lattice spacing because of the smaller atomic radius of the dopant atom compared to the host material [37, 38]. The absence of other noticeable peaks indicates the phase pure formation of CoS and its transformation into S, N-Co_9S_8. Further, the Raman spectra of the CoS, N-Co_9S_8, and S, N-Co_9S_8 catalyst were recorded to elucidate the material fingerprint (Figure 2(d)). The pristine CoS catalyst (black spectrum) shows the characteristic Raman vibrational mode of Co-S (298 and 344 cm^{-1}), E_g (474 cm^{-1}), F_{2g} (519 cm^{-1}), and A_{1g} (675 cm^{-1}), whereas the N-Co_9S_8 (green spectrum) and S, N-Co_9S_8 catalyst (red spectrum) shows two Co-S vibrational modes similar to the pristine CoS catalyst, among the four Raman peaks [31]. However, these two initial peaks were slightly right-shifted (298 to 304 cm^{-1} and 344 to 351 cm^{-1}, respectively) compared with the vibrational mode of CoS. The remaining two peaks originated from the S-S symmetric stretching (479 cm^{-1}) and the lattice vibrations (614 cm^{-1}) of Co-cations on the surface of S, N-Co_9S_8 [39]. The blue shift in the Co-S vibrational peak could be a result of induced compressive strain associated with compressive stress, which originates from the presence of heteroatoms in the unstressed crystal structure. This analysis is consistent with the XRD result.

FE-SEM images were recorded to investigate the effect of the material phase on the morphological structure of the prepared cobalt species. Figure 3 shows the FE-SEM images of the CoS and S,N-Co_9S_8 catalyst electrodes. For

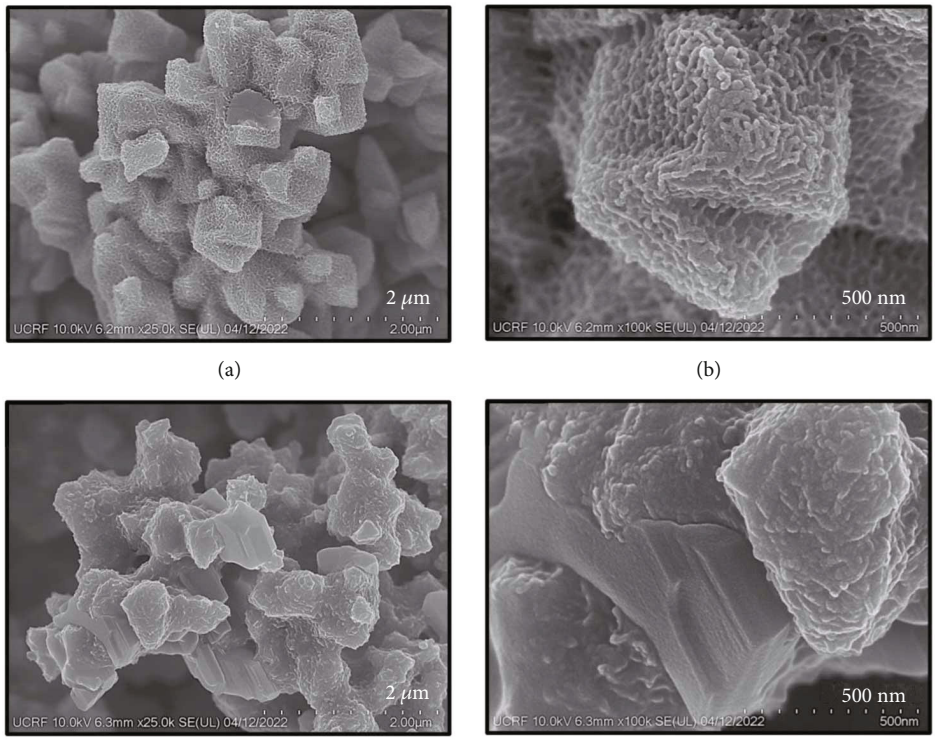

Figure 3: FE-SEM images of the (a, b) CoS and (c, d) S,N-Co_9S_8 catalyst electrodes at low and high magnifications.

comparison, the morphology of the intermediate-state N-Co_9S_8 electrode film was also recorded (Figure S1, Supporting Information). Figure 3(a) shows the FE-SEM image of the CoS catalyst electrode, revealing an accumulated polyhedral structure grown vertically with several void spaces on the 3D NF substrate that might be due to the uneven growth of the active species in the hydrothermal process. These voids assist in the relaxed reversing channel for the electrolyte and lead to the increment in the number of active sites, which is helpful in improving the catalytic efficacy [40]. A well-defined flake-like characteristic embossed texture is observed on the surface of these polyhedral structures (Figure 3(b)). The flake-like texture is less prominent for the N-Co_9S_8 (supporting Figure S1) electrode film. Although, the S,N-Co_9S_8 catalyst electrode maintains similar morphological structure as that of the CoS. However, the surface texture and topography changed significantly. A rough embossed texture is observed on the polyhedral surface. In addition to material morphology, the constituent element's chemical composition and their distribution for the CoS, N-Co_9S_8, and S,N-Co_9S_8 catalyst electrodes were analyzed by means of an EDS technique. Supporting Figure S2 shows the obtained EDS spectra and the mapped atomic chemical compositions of the constituent elements, respectively. The obtained chemical compositions are summed up in the Tables (inset of supporting Figures S2A, B), revealing the stoichiometric atomic percentage of all constituent elements in the prepared catalyst electrodes.

The local crystal structure, lattice orientation, and the presence of constituent elements at the atomic level were further confirmed by TEM, HR-TEM, and HAADF-STEM line scanning image analyses. Figure 4(a) shows the TEM image of the CoS which consists of numerous interconnected small particles (dark region) and voids (grey region), confirming its porous polyhedral architecture. The HR-TEM image (Figure 4(b)) reveals a random orientation of local planes, which are indexed in the magnified view. The interplanar lattice spacing (d-spacing) of 0.29 ± 0.01 and 0.25 ± 0.01 nm are associated with the reflection of the (100) and (002) planes of hexagonal CoS (JCPDS card no. 75-0605), respectively. Moreover, the HAADF-STEM line scanning (Figure 4(c)) reveals the stoichiometric existence of the constituent Co and S elements. The size of the interconnected particles increases for the N-Co_9S_8 (Figure 4(d)) possibly due to the fusion of smaller particles during high temperature annealing. The N-Co_9S_8 reveals the d-spacing of 0.18 ± 0.01 and 0.22 ± 0.01 nm (Figure 4(e)), which are associated with the reflection of the (440) and (331) planes of the cubic Co_9S_8 (JCPDS card no. 86-2273), respectively. The HAADF-STEM line scanning of the N-Co_9S_8 (Figure 4(f)) confirms the presence of N in the Co_9S_8 structure. The TEM image for the S,N-Co_9S_8 (Figure 4(g)) reveals that accumulated particles size in the polyhedral structure decreases significantly compared to the N-Co_9S_8. This could be possibly due to the recrystallization upon anion-exchange and is consistent with the deformed polyhedral structure observed in the FE-SEM image of the S,N-Co_9S_8 (Figure 3(c) and 3(d)). The N-Co_9S_8 also shows a clear lattice fringe pattern (Figure 4(h)) with the d-spacing of 0.28 ± 0.01 and 0.18 ± 0.01 nm, which are related to the reflection of the (222) and (440) planes, respectively. Moreover,

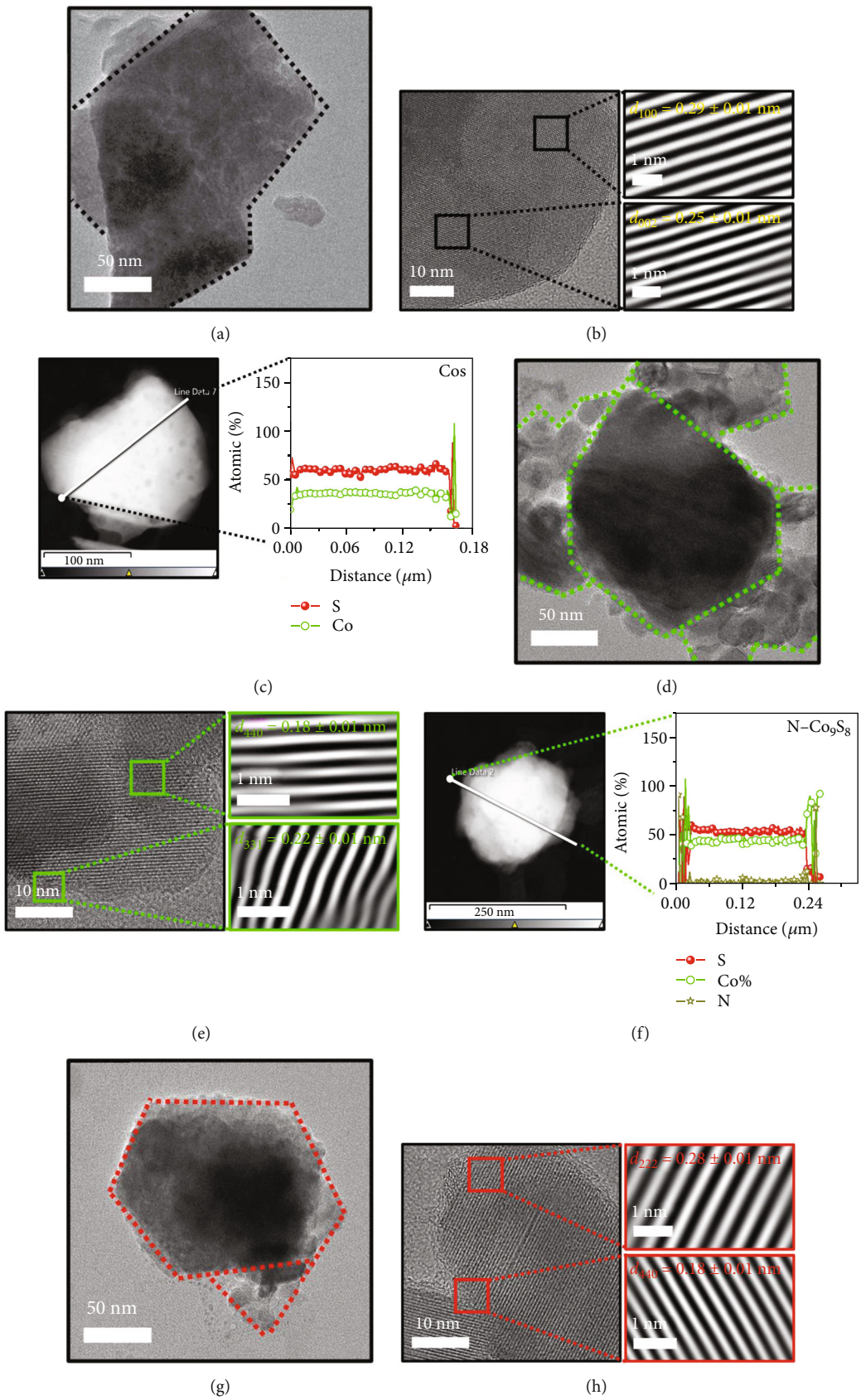

Figure 4: Continued.

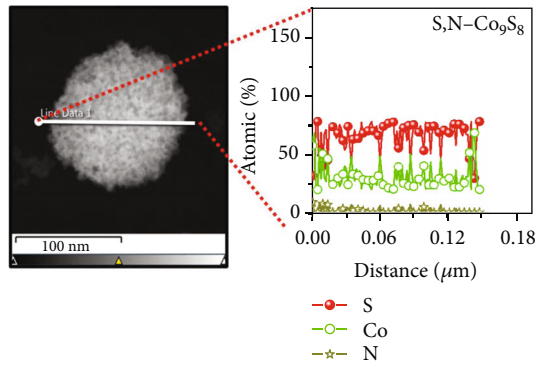

FIGURE 4: (a, d, g) TEM, (b, e, h) HR-TEM, and (c, f, i) HAADF-STEM line scan mapping images for the CoS, N-Co_9S_8, and S,N-Co_9S_8 catalysts.

the HAADF-STEM line scanning of the N-Co_9S_8 (Figure 4(i)) further confirms the existence of Co, S, and N elements similar to the N-Co_9S_8 (Figure 4(f)) and reveals increased S content.

To further support the above mentioned XRD, Raman, FE-SEM, EDS, TEM, and HR-TEM analyses, XPS measurement for the CoS, N-Co_9S_8, and S,N-Co_9S_8 catalyst electrodes was performed. Figure 5(a) shows the full-range survey spectra of the prepared cobalt species. The additional C 1 s and O 1 s peak in survey are associated with the carbon contaminant inside the vacuum chamber and the adsorbed oxygen on the film from the environment [41–44]. The Gaussian curve fitting model was used to fit the narrow range XPS emission spectra [45]. The Co 2p spectrum of the CoS catalyst electrode (Figure 5(b)) shows a total of four emission peaks at 781.31, 788.30 (satellite; Sat.), 797.30, and 804.29 (Sat.) eV. The low energy peaks (initial two) are related to Co $2p_{3/2}$, and the high energy peaks (later two) are associated with the Co $2p_{1/2}$ emissions of cobalt. The spin-energy separation of 15.99 eV (≈16.00 eV; Co $2p_{1/2}$–Co $2p_{3/2}$) reveal the presence of the Co^{2+} state [46]. The S 2p XPS spectrum (Figure 5(c)) of the CoS catalyst electrode shows two characteristic peaks at 162.80 and 163.99 eV after the deconvolution of a broad peak, which are associated with the characteristic S $2p_{3/2}$ and S $2p_{1/2}$ emissions. The spin-energy separation of 1.19 eV (S $2p_{1/2}$–S $2p_{3/2}$) assured the divalent state of sulfur (S^{2-}) bounded to Co^{2+} ions of cobalt in the CoS structure. The N-Co_9S_8 and S,N-Co_9S_8 catalyst electrodes also exhibits identical spin-energy separation for Co 2p and S 2p. However, the Co 2p and S 2p spectra were slightly right-shifted compared with the pristine CoS catalyst electrode (Figure 5(b) and 5(c)). This rigid binding energy shift for N-Co_9S_8 compared with CoS is associated with N-doping and the Co 2p and S 2p peak positions remains almost intact after the incorporation of S in the N-Co_9S_8 (i.e., the S,N-Co_9S_8 structure). The blue shift in the binding energy is a result of the lower concentration of electrons around the cobalt nuclei because of the higher electronegativity and stronger electron trapping capability of nitrogen compared with that of sulfur in the N-Co_9S_8 [37]. Moreover, the Co 2p spectra for the N-Co_9S_8 and S,N-Co_9S_8 catalyst electrodes reveal additional deconvoluted peaks originating from the Co-N and Co-O binding states compared with that of the CoS catalyst electrode [47]. Furthermore, the S 2p peak intensity of the N-Co_9S_8 catalyst electrode decreased slightly compared with that of the pristine CoS after high temperature annealing in ambient N_2. This spectrum (Figure 5(c)) reveals an additional peak related to SO_x^{n-} that could have originated from the strong interaction of the adsorbed oxygen with sulfur in air to form sulfate [31, 48]. The SO_x^{n-} peak became less prominent after the anion-exchange process, whereas the intensity of the S 2p peaks significantly increased compared with the N-Co_9S_8 catalyst electrode, indicating the higher S content in the S,N-Co_9S_8 structure. In addition, the N-Co_9S_8 and S,N-Co_9S_8 catalyst electrodes shows an additional N 1 s peak in the survey spectrum (Figure 5(a)). The high-resolution N 1 s spectra (Figure 5(d)) exhibits a broad peak related to Co-N bonding within the Co_9S_8 structure originating from the replacement of S by the N dopant in the lattices [37, 49, 50]. XPS analysis further confirms the formation of the CoS structure and its complete transformation into N-Co_9S_8 and S,N-Co_9S_8.

The electrochemical OER and HER performance of the prepared cobalt species were examined thoroughly via LSV, with the chronopotentiometric voltage-step profile being a function of the current density, chronopotentiometric stability, and Nyquist impedance curve analyses. Figure 6(a) shows the obtained OER LSV curves that were recorded in a potential window range between 0.00 and 1.00 V (vs. SCE) for the CoS, N-Co_9S_8, and S,N-Co_9S_8 catalysts measured at 5.0 mV s^{-1} in alkaline 1.0 M KOH electrolyte. All of the obtained polarization curves were initially converted into the reversible hydrogen electrode (RHE) reference scale and then $JR_{corrected}$ with the help of solution resistance (R_S) and by using the following equations: [31, 51, 52]

$$\begin{aligned} E_{RHE} &= E_{SCE} + E^{\circ}{}_{SCE} + 0.059 \times pH(\mathrm{KOH}), \\ E_{RHE\,JRcorrected} &= E_{RHE} - (J \times R_S), \\ \eta &= E_{RHE} - 1.23(\mathrm{OER}), \end{aligned} \tag{2}$$

where E_{SCE} is the obtained potential in the reference SCE electrode scale and $E^{\circ}{}_{SCE}$ is the standard potential of the SCE at room temperature. The S,N-Co_9S_8 catalyst

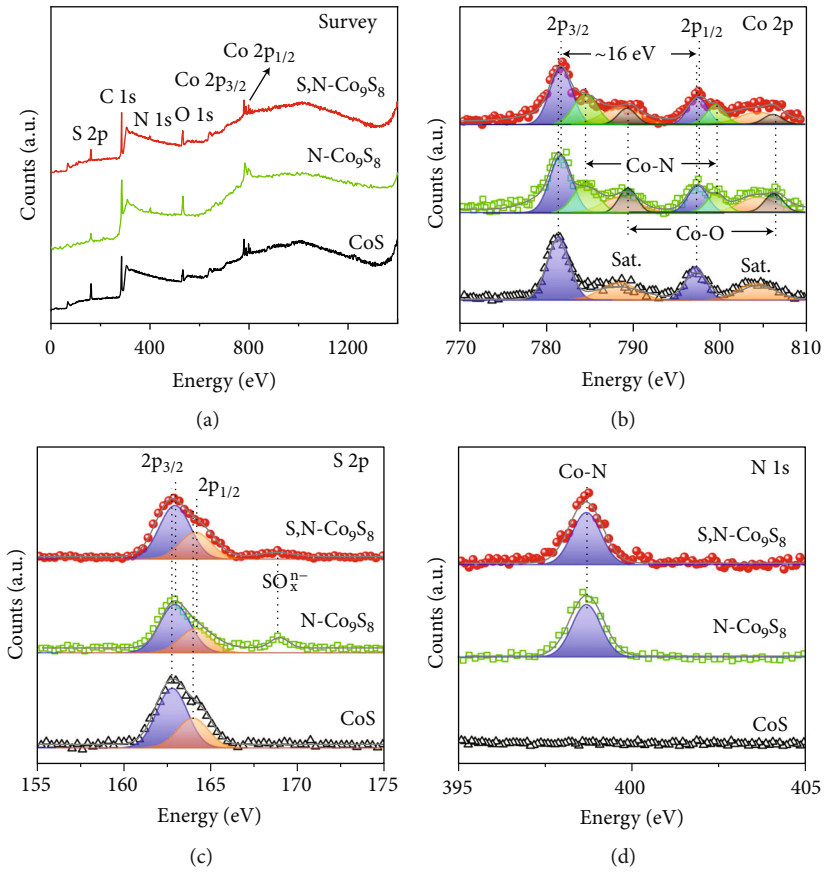

FIGURE 5: (a) XPS survey spectra for the CoS, N-Co_9S_8, and S,N-Co_9S_8 catalyst measured within a binding energy range of 0 and 1400 eV. High-resolution XPS emission spectra: (b) Co 2p, (c) S 2p, and (d) N 1 s for the CoS, N-Co_9S_8, and S,N-Co_9S_8 catalysts. All of these high-resolution XPS spectra were calibrated with the C 1 s peak of the carbon contaminant and deconvoluted using a Gaussian curve fitting model.

demonstrates excellent electrocatalytic OER activity by attaining a low overpotential of 244 mV (vs. RHE) at a driving current density of 10 mA cm^{-2}, whereas the pristine CoS and N-Co_9S_8 catalysts attains an overpotential value of 292 and 259 mV at the same current density value, respectively. For comparison, polarization curves for the RuO_2 and bare NF substrate (supporting Figure S3A) were also recorded at the same experimental conditions. An almost inactive OER activity was observed for the bare NF substrate, revealing a large overpotential of 442 mV at an applied current density of 10 mA cm^{-2}. The enhanced electrocatalytic OER activity of the S,N-Co_9S_8 catalyst is aroused from improved conductivity and elevated electrocatalytically active sites, which results in efficient electron/ion transport and better intrinsic reaction kinetics (Figure S4–S7 and Table S1, Supporting Information). The electrocatalytic OER performance of the S,N-Co_9S_8 catalyst is relatively comparable to those of a cobalt sulfide-based catalyst reported in the literature (Figure 2(a) and Table S2).

The electrochemical reaction kinetics of the catalyst material was further assessed from the associated Tafel curve slope. Figure 6(b) shows the associated Tafel plots for the CoS and S,N-Co_9S_8 catalyst, which were obtained from the linear portion of the polarization curves. The Tafel curves were fitted using the Tafel equation as follows: [33, 53–55]

$$\eta = \beta \times \log(J) + \alpha, \tag{3}$$

where β, J, and α are the Tafel slope, current density, and fitting parameter, respectively. The S,N-Co_9S_8 catalyst reveals a smaller Tafel slope of 47 mV dec^{-1}, which is considerably lower than the Tafel slope of the pristine CoS catalyst (70 mV dec^{-1}), N-Co_9S_8 (66 mV dec^{-1}), and RuO_2 (65 mV dec^{-1}) catalysts. The smallest Tafel slope value of the S,N-Co_9S_8 catalyst is indicative of the catalyst's superior intrinsic reaction kinetics compared with the pristine CoS and the N-Co_9S_8 catalysts and is supported by the turnover frequency (TOF) analysis (Supporting Figure S6A). Generally, the OER process requires a four-electron transfer for the reaction mechanism, while the transfer of one electron occurred at each step, leading to sluggish reaction kinetics for the OER process. A Tafel slope of 40 mV dec^{-1} indicates that a two-electron transfer is the rate-determining step, a Tafel slope of 60 mV dec^{-1} is linked to the rate-limiting step that follows the first electron transfer, and a Tafel slope of 120 mV dec^{-1} is associated with the turnover-limiting single electron transfer process that occurs in the catalyst's resting state [56, 57]. The variation in the Tafel slope with increasing potential could be a result of change in the potential response following the

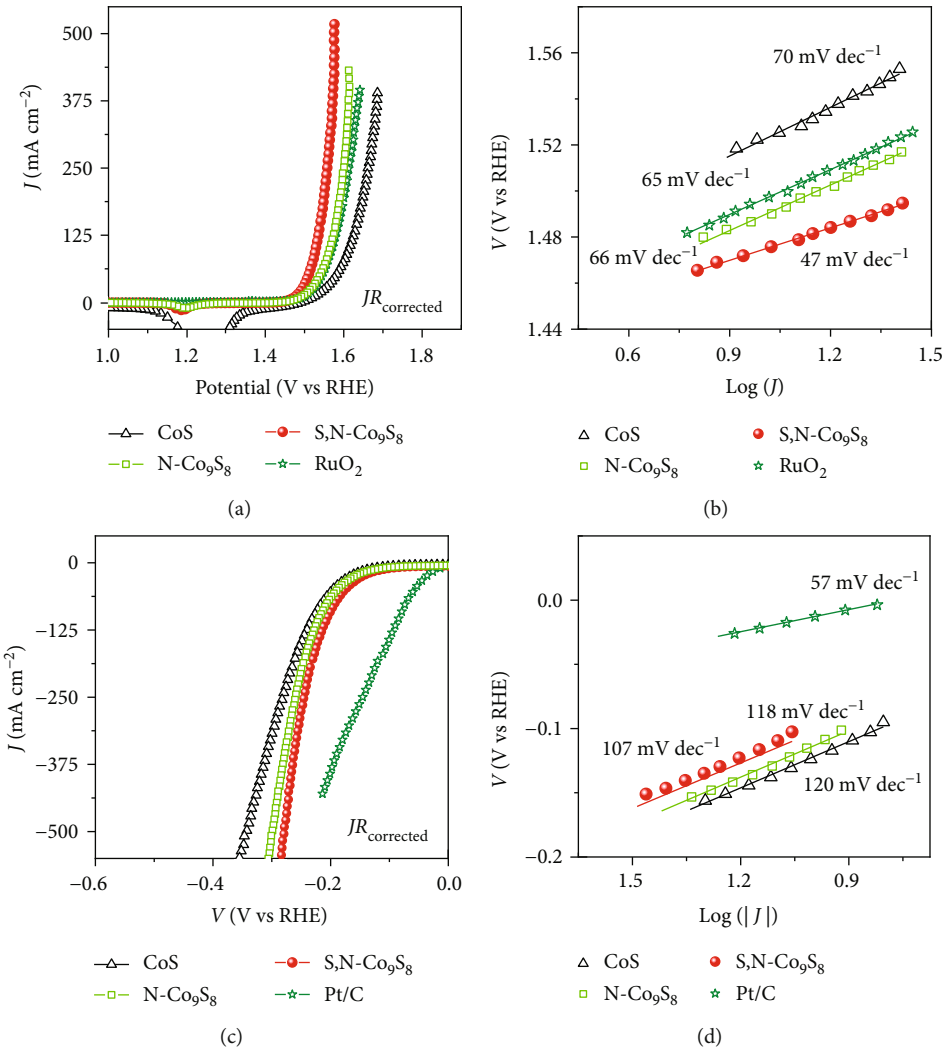

Figure 6: Electrocatalytic OER and HER activity of the CoS, N-Co_9S_8, and S,N-Co_9S_8 catalysts. (a) OER polarization curves, (b) the associated Tafel plots, (c) HER polarization curves, and (d) the corresponding Tafel plots of the prepared catalysts. All of the polarization curves were obtained at 5.0 mV s^{-1} in an alkaline KOH (1.0 M) electrolyte. For comparison purposes, RuO_2 and Pt/C were also tested.

adsorption of reaction intermediates or a change in the rate-determining step [58, 59]. The S,N-Co_9S_8 catalyst reveals the smallest Tafel slope, which is crucial for efficient electrocatalytic OER activity. The low Tafel slope is most likely due to the second reaction step being rate-determining. Moreover, the low Tafel slope also indicates that strong surface intermediate adsorption during the initial step hindering the subsequent step, which turn out to be rate-limiting [59]. In contrast, the CoS and N-Co_9S_8 catalysts trails the rate-limiting step. The obtained electrocatalytic OER activity for the CoS, N-Co_9S_8, and S,N-Co_9S_8 catalysts were highly reproducible in independent and sequential catalyst test (Figure S8A, Supporting Information).

In addition to the low overpotential of the S,N-Co_9S_8 catalyst obtained at 10 mA cm^{-2}, a quantitative potential response analysis using the chronopotentiometric test was performed at low and high current rates. Supporting Figure S9A shows the potential-step profile being a function of the current density. The driven current density was kept constant for an interval of 20 min at each step, and a static voltage response was obtained at each applied current rate. A linear relationship was observed between "η" and "J" (Figure S9B, Supporting Information). The S,N-Co_9S_8 catalyst maintains a smaller potential response compared with the pristine CoS catalyst at each current rate. This is the indicative of efficient electron/ion transport throughout the porous polyhedral structure, robust adhesion, and excellent conductivity of the catalysts. In addition to the electrocatalytic OER activity, catalyst stability in alkaline conditions is also a crucial factor to be examined for the real time application of the active catalyst. Supporting Figure S9C shows the long-term chronopotentiometric stability for the S,N-Co_9S_8 catalyst measured at various current rates of 10, 50, and 100 mA cm^{-2}. The S,N-Co_9S_8 catalyst maintains a steady potential response during the continuous 50 h chronopotentiometric electrolysis after a minor potential

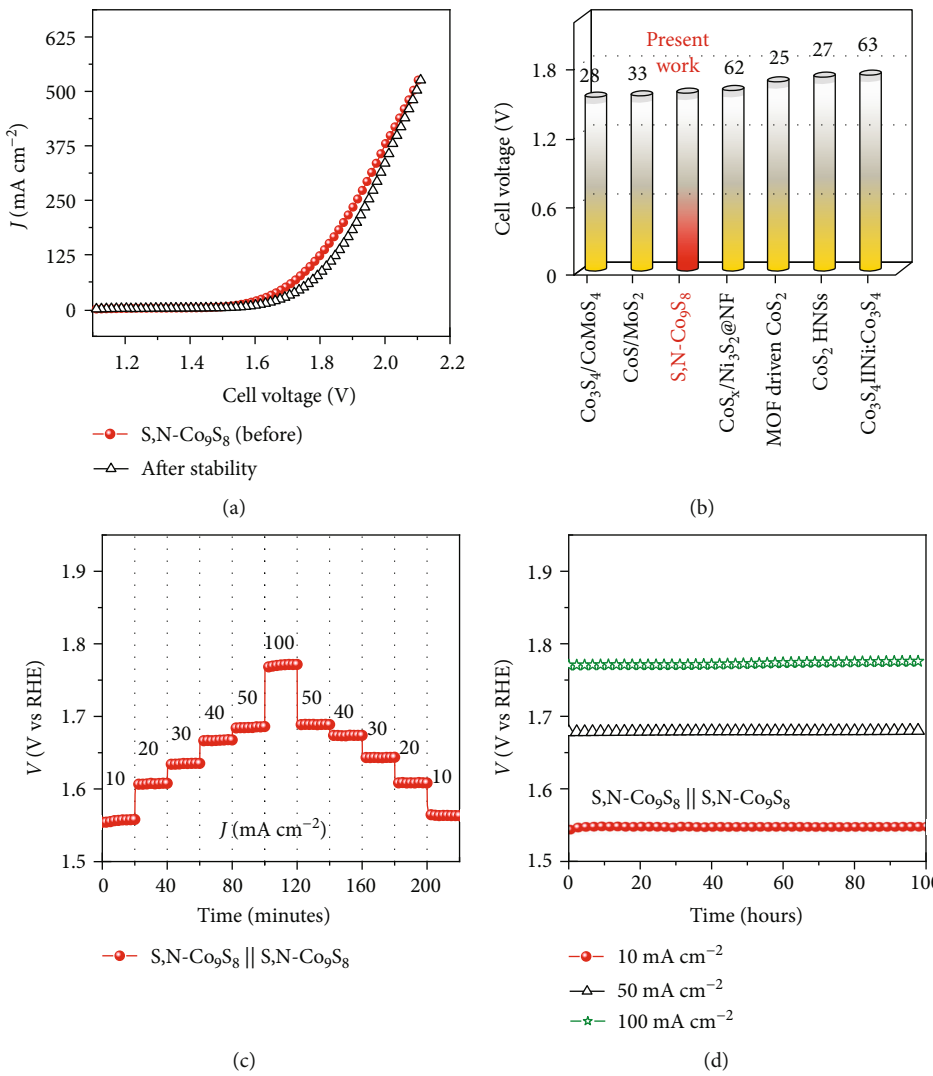

FIGURE 7: The overall electrolysis performance of the S,N-Co_9S_8 as a bifunctional catalyst in 1.0 M KOH electrolyte medium. (a) Polarization curves obtained at 5.0 mV s^{-1} before and after long-term chronopotentiometric stability. (b) Comparative full-cell voltage of our S,N-Co_9S_8||S,N-Co_9S_8 bifunctional catalyst and previously reported cobalt-sulfide-based catalysts. (c) Voltage-step profile and (d) chronopotentiometric stabilities measured at 10, 50, and 100 mA cm^{-2}.

loss of 0.37% in the initial stage. The increase in the potential may be due to the partial transformation of the S,N-Co_9S_8 surface into CoOOH during the electrooxidation process (reversible redox reaction; Eq. (4)–(6)), as evidenced by the presence of mixed Co^{2+}/Co^{3+} oxidation states. This results in the increase in the O 1 s peak intensity, as shown in the post-stability XPS emission spectra (supporting Figure S10A-C) [4, 7, 10, 26]. The post-OER stability XRD spectrum (supporting Figure S10D) also exhibits two small additional diffraction peaks related to the CoOOH phase and this phase transformation is further supported by the HR-TEM data measured after the chronopotentiometric OER stability test (supporting Figure S11), revealing the reflection of the (012) plane associated with the CoOOH phase [60]. This transformation leads to a slightly deformed morphological structure, as shown in the FE-SEM images (supporting Figure S12) recorded after long-term chronopotentiometric electrolysis. Thus, based on the post-stability XPS, XRD, HR-TEM, and FE-SEM analyses, the S,N-Co_9S_8 core with a thin CoOOH shell is confirmed to be the electrocatalytically active phase during the OER process [4, 6, 26]. Nonetheless, an almost identical Nyquist impedance and polarization curves before and after the long-term chronopotentiometric electrolysis (Figures S7B, S9D, Supporting Information) confirms its excellent endurance throughout the stability test for the electrocatalytic OER in alkaline KOH medium.

$$Co_9S_8 + 18(OH)^- \leftrightarrow 9\,Co(OH)_2 + 8\,S^{2-} + 2\,e^-, \quad (4)$$

$$Co(OH)_2 + (OH)^- \leftrightarrow CoOOH + H_2O + e^-, \quad (5)$$

$$CoOOH + (OH)^- \leftrightarrow CoO_2 + H_2O + e^-. \quad (6)$$

Since the electrocatalytic HER performance is another important factor for evaluating the overall water splitting,

the HER activity of each catalyst is assessed on the basis of cathodic polarization curve. Figure 6(c) shows the J $R_{corrected}$ polarization curves for the CoS, N-Co_9S_8, and S,N-Co_9S_8 catalysts as well as for the bare NF substrate (supporting Figure S3C) and Pt/C catalyst measured at a scan rate of 5.0 mV s^{-1} in 1.0 M KOH electrolyte. The S,N-Co_9S_8 catalyst further reveals an excellent electrocatalytic HER activity, achieving a small overpotential of −92 mV (vs. RHE; $\eta = E_{RHE\ JRcorrected}$) at 10 mA cm^{-2} [61], which is quite comparable to the overpotential reported in previous literatures (Figure 2(b) and Table S3) and reproduceable within an adequate tolerable range (supporting Figure S8B). Notably, the overpotentials of −123, −114, and −342 mV are required to achieve the same current density for the CoS, N-Co_9S_8, and NF substrate, respectively. It is well known that the Pt/C is a state-of-the-art catalyst because of its electrocatalytic HER activity. For comparison, a commercially available Pt/C was used, which shows an overpotential of −13 mV at 10 mA cm^{-2}. However, at high a current value, the S,N-Co_9S_8 catalyst activity is competing well with the Pt/C catalyst, suggesting that the S,N-Co_9S_8 catalyst activity is more favourable for HER process. This could be linked to the efficient inherent kinetics, which is supported by the Tafel, ECSA-based LSV, and TOF curve analyses (Figure 6(d), Figure S6 and Table S4, Supporting Information). As shown in Figure 6(d), the S,N-Co_9S_8 catalyst reveals a Tafel slope of 107 mV dec^{-1} (Volmer mechanism), which is less than those of the CoS (120 mV dec^{-1}) and the bare NF substrate (134 mV dec^{-1}), indicating the faster H_2 evolution on the S,N-Co_9S_8 catalyst surface [33]. The superior HER performance of the S,N-Co_9S_8 catalyst is associated with the incorporation of S and N into the Co_9S_8 catalyst structure, which reduces the activation barrier and results in enhanced electrocatalytic HER activity [31, 33].

A multistep chronopotentiometric electrolysis was performed to elucidate the quantitative voltage response of the prepared catalysts. Supporting Figure S13A shows the measured multistep voltage profile measured as a function of the current rate. As expected, the S,N-Co_9S_8 catalyst shows a steady potential voltage response, revealing the linear potential response with an applied current density ("$\eta\ \alpha\ J$"; Supporting Figure S13B) and maintains the lowest voltage response at each driven current rate. Furthermore, the chronopotentiometry test was conducted to evaluate the endurance of the catalyst during the long-term stabilities. Supporting Figure S13C shows the chronopotentiometric electrolysis curve for the S,N-Co_9S_8 catalyst measured up to 50 h at various current densities. The S,N-Co_9S_8 catalyst shows static potential response at each applied current rate without underlying the material morphology and surface topography (Figures S12C, D, Supporting Information), revealing its excellent endurance throughout the chronopotentiometric electrolysis test, and demonstrating the excellent electrocatalytic HER activity in the 1.0 M KOH electrolyte medium [3, 4, 31]. This analysis is further supported by the Nyquist impedance and polarization curve recorded before and after the long-term chronopotentiometric stability (Figures S7B, S13D, Supporting Information).

Due to its excellent electrocatalytic OER and HER activity, the bifunctional activity of the S,N-Co_9S_8 catalyst was investigated in a 1.0 M KOH electrolyte using a two-electrode electrolyzer cell. The S,N-Co_9S_8 catalyst served as both the anode (OER catalyst) and cathode (HER catalyst) for the electrolyzer. Figure 7(a) presents the polarization curves for the bifunctional S,N-Co_9S_8||S,N-Co_9S_8 measured in a voltage window range of 1.1–2.2 V at a scan rate of 5.0 mV s^{-1}, producing an electrolyzer cell voltage of 1.549, 1.693, and 1.772 V at 10, 50, and 100 mA cm^{-2}, respectively. Figure 7(b) displays the comparative full-cell performance of our S,N-Co_9S_8||S,N-Co_9S_8 bifunctional catalyst and various metal sulfide-based catalysts reported at 10 mA cm^{-2} in an alkaline KOH electrolyte (1.0 M) medium [25, 27, 28, 33, 62, 63]. The obtained bifunctional cell voltage was competitive with that of the cobalt sulfide-based catalysts. The reliability of the S,N-Co_9S_8||S,N-Co_9S_8 bifunctional catalyst was confirmed by evaluating the full-cell electrochemical activity under the same experimental conditions. The fabricated electrolyzer cell demonstrated electrolysis activity within a suitable range (Supporting Figure S8C). A linear relationship between the potential and current density was also observed in the voltage-step profile (Figure 7(c)), for the S,N-Co_9S_8||S,N-Co_9S_8 bifunctional electrolyzer cell. This electrolyzer cell also exhibited a steady potential response (~100%; Figure 7(d)), highlighting its long-term chronopotentiometric stability, as illustrated by the post-stability polarization curve (Figure 7(a)). The excellent endurance throughout the long-term chronopotentiometric test is a result of synergy and mutual interaction between the heteroatoms, varied electronic structure, robust adhesion, high mechanical strength, enhanced conductivity, and large catalytically active sites, which results in efficient electron/ion transport and improved electrochemical reaction kinetics compared to the as deposited catalyst material.

4. Conclusion

In summary, a cost-effective synthesis of unique freestanding polyhedral-like CoS topography with microporous architecture has been accomplished via a facile hydrothermal process. An active S,N-Co_9S_8 catalyst was obtained from the pristine CoS catalyst through nitrogen annealing followed by anion-exchange process, and it demonstrates superior electrocatalytic OER and HER activities in alkaline KOH (1.0 M) medium. The optimized S,N-Co_9S_8 catalyst exhibits excellent bifunctional electrocatalytic OER (244 mV) and HER (−92 mV) activities at 10 mA cm^{-2} with comparatively enhanced intrinsic reaction kinetics than that of the CoS catalyst. The catalytic activity of the S,N-Co_9S_8 catalyst is even compared with the RuO_2 and Pt/C catalysts and high current densities. Moreover, S,N-Co_9S_8 bifunctional catalyst demonstrates a steady potential response and excellent stability endurance throughout 50 h for both OER and HER process at various current densities. The excellent electrocatalytic performance of the S,N-Co_9S_8 catalyst is aroused from the enhancement in the electron transfer and ion transport at the electrolyte interface along with

improved material conductivity and enhanced electrocatalytically active surface sites, resulting in the elevated intrinsic reaction kinetics (Tafel, ECSA corrected LSV, and TOF analyses) after the heteroatom incorporation that could have changed the active catalyst surface chemistry. This universal approach could be helpful for the development of highly efficient nonnoble metal-based catalysts with excellent electrocatalytic activities.

Data Availability

The data used to support the findings of this study are available from the corresponding author upon request.

Conflicts of Interest

The authors declare no competing financial interests.

Acknowledgments

This study was supported by the National Research Foundation of Korea (Grant nos. 2021R1A2B5B01001796, 2021R1A2C1006113, and 2021R1A4A5031805).

Supplementary Materials

Supporting Data Information (Figures S1-S13 and Table S1-S4) associated with this article can be found in the supplementary materials. *(Supplementary Materials)*

References

[1] J. A. Turner, "Sustainable hydrogen production," *Science*, vol. 305, no. 5686, pp. 972–974, 2004.

[2] S. Sekar, A. T. A. Ahmed, S. M. Pawar et al., "Enhanced water splitting performance of biomass activated carbon-anchored WO_3 nanoflakes," *Applied Surface Science*, vol. 508, article 145127, 2020.

[3] S. M. Pawar, A. T. A. Ahmed, C. H. Lee et al., "Experimental and theoretical insights into transition-metal (Mo, Fe) Codoping in a bifunctional nickel phosphide microsphere catalyst for enhanced overall water splitting," *ACS Applied Energy Materials*, vol. 4, no. 12, pp. 14169–14179, 2021.

[4] A. T. A. Ahmed, S. M. Pawar, A. I. Inamdar, H. Kim, and H. Im, "A morphologically engineered robust bifunctional $CuCo_2O_4$ Nanosheet catalyst for highly efficient overall water splitting," *Advanced Materials Interfaces*, vol. 7, no. 2, article 1901515, 2020.

[5] C. Bathula, A. T. A. Ahmed, A. Kadam et al., "Multi-functional Co_3O_4 embedded carbon nanotube architecture for oxygen evolution reaction and benzoin oxidation," *Journal of Molecular Liquids*, vol. 343, article 117616, 2021.

[6] A. T. A. Ahmed, B. Hou, H. S. Chavan et al., "Self-assembled nanostructured $CuCo_2O_4$ for electrochemical energy storage and the oxygen evolution reaction via morphology engineering," *Small*, vol. 14, no. 28, article 1800742, 2018.

[7] Y. Jo, S. Cho, J. Seo et al., "Experimental and theoretical insights into the borohydride-based reduction-induced metal interdiffusion in Fe-Oxide@NiCo2O4for enhanced oxygen evolution," *ACS Applied Materials & Interfaces*, vol. 13, no. 45, pp. 53725–53735, 2021.

[8] S. Anantharaj, S. R. Ede, K. Sakthikumar, K. Karthick, S. Mishra, and S. Kundu, "Recent trends and perspectives in electrochemical water splitting with an emphasis on sulfide, selenide, and phosphide catalysts of Fe, Co, and Ni: a review," *ACS Catalysis*, vol. 6, no. 12, pp. 8069–8097, 2016.

[9] L. Han, S. Dong, and E. Wang, "Transition-metal (co, Ni, and Fe)-based electrocatalysts for the water oxidation reaction," *Advanced Materials*, vol. 28, no. 42, pp. 9266–9291, 2016.

[10] S. M. Pawar, B. S. Pawar, B. Hou et al., "Self-assembled two-dimensional copper oxide nanosheet bundles as an efficient oxygen evolution reaction (OER) electrocatalyst for water splitting applications," *Journal of Materials Chemistry A*, vol. 5, no. 25, pp. 12747–12751, 2017.

[11] X. Zhu, J. Dai, L. Li et al., "Hierarchical carbon microflowers supported defect-rich Co_3S_4 nanoparticles: an efficient electrocatalyst for water splitting," *Carbon*, vol. 160, pp. 133–144, 2020.

[12] J. F. Qin, J. H. Lin, T. S. Chen et al., "Facile synthesis of V-doped CoP nanoparticles as bifunctional electrocatalyst for efficient water splitting," *Journal of Energy Chemistry*, vol. 39, pp. 182–187, 2019.

[13] Y. L. Tong, L. Xing, M. Z. Dai, and X. Wu, "Hybrid Co_3O_4@-Co_9S_8 electrocatalysts for oxygen evolution reaction," *Frontiers in Materials*, vol. 6, 2019.

[14] Y. Dong, J. Ran, Q. Liu, G. Zhang, X. Jiang, and D. Gao, "Hydrogen-etched CoS2 to produce a Co9S8@CoS2 heterostructure electrocatalyst for highly efficient oxygen evolution reaction," *RSC Advances*, vol. 11, no. 48, pp. 30448–30454, 2021.

[15] X. Feng, Q. Jiao, T. Liu et al., "Facile synthesis of Co_9S_8 hollow spheres as a high-performance electrocatalyst for the oxygen evolution reaction," *ACS Sustainable Chemistry & Engineering*, vol. 6, no. 2, pp. 1863–1871, 2018.

[16] C. Sun, J. Ding, H. Wang et al., "Cobalt sulfides constructed heterogeneous interfaces decorated on N,S-codoped carbon nanosheets as a highly efficient bifunctional oxygen electrocatalyst," *Journal of Materials Chemistry A*, vol. 9, no. 24, pp. 13926–13935, 2021.

[17] H. Liu, C. Y. Xu, Y. Du et al., "Ultrathin Co_9S_8 nanosheets vertically aligned on N,S/rGO for low voltage electrolytic water in alkaline media," *Scientific Reports*, vol. 9, no. 1, article 1951, 2019.

[18] J. Hao, W. Yang, Z. Huang, and C. Zhang, "Superhydrophilic and superaerophobic copper phosphide microsheets for efficient electrocatalytic hydrogen and oxygen evolution," *Advanced Materials Interfaces*, vol. 3, no. 16, article 1600236, 2016.

[19] S. H. Koo, D. J. Li, T. Yun et al., "Cobalt based Nanoparticles embedded reduced graphene oxide aerogel for hydrogen evolution electrocatalyst," *Particle & Particle Systems Characterization*, vol. 36, no. 7, article 1900090, 2019.

[20] J. Huang, D. Hou, Y. Zhou et al., "MoS_2 nanosheet-coated CoS_2 nanowire arrays on carbon cloth as three-dimensional electrodes for efficient electrocatalytic hydrogen evolution," *Journal of Materials Chemistry A*, vol. 3, no. 45, pp. 22886–22891, 2015.

[21] Z. Zhou, N. Mahmood, Y. Zhang et al., "CoP nanoparticles embedded in P and N co-doped carbon as efficient bifunctional electrocatalyst for water splitting," *Journal of Energy Chemistry*, vol. 26, no. 6, pp. 1223–1230, 2017.

[22] S. S. Raya, A. S. Ansari, and B. Shong, "Molecular adsorption of NH_3 and NO_2 on Zr and Hf Dichalcogenides (S, Se, Te)

monolayers: a density functional theory study," *Nanomaterials*, vol. 10, no. 6, article 1215, 2020.

[23] X. Qiu and C. Burda, "Chemically synthesized nitrogen-doped metal oxide nanoparticles," *Chemical Physics*, vol. 339, no. 1-3, pp. 1–10, 2007.

[24] A. S. Ansari, J. W. Han, and B. Shong, "Intermediates for catalytic reduction of CO_2 on p-block element surfaces," *Journal of Industrial and Engineering Chemistry*, vol. 96, pp. 236–242, 2021.

[25] I. K. Ahn, W. Joo, J. H. Lee et al., "Metal-organic framework-driven porous cobalt disulfide Nanoparticles fabricated by gaseous sulfurization as bifunctional electrocatalysts for overall water splitting," *Scientific Reports*, vol. 9, no. 1, p. 19539, 2019.

[26] A. T. A. Ahmed, S. M. Pawar, A. I. Inamdar, H. Im, and H. Kim, "Fabrication of FeO@$CuCo_2S_4$ multifunctional electrode for ultrahigh-capacity supercapacitors and efficient oxygen evolution reaction," *International Journal of Energy Research*, vol. 44, no. 3, pp. 1798–1811, 2020.

[27] X. Ma, W. Zhang, Y. Deng, C. Zhong, W. Hu, and X. Han, "Phase and composition controlled synthesis of cobalt sulfide hollow nanospheres for electrocatalytic water splitting," *Nanoscale*, vol. 10, no. 10, pp. 4816–4824, 2018.

[28] Y. Song, W. Sha, T. Jiao et al., "Interface-engineered Co3S4/CoMo2S4 nanosheets as efficient bifunctional electrocatalysts for alkaline overall water splitting," *Nanotechnology*, vol. 32, no. 45, article 455706, 2021.

[29] M. Chauhan and S. Deka, "Hollow Cobalt Sulfide Nanoparticles: A robust and low-cost pH-universal oxygen evolution electrocatalyst," *ACS Applied Energy Materials*, vol. 3, no. 1, pp. 977–986, 2020.

[30] K. Rehman, S. Airam, X. Lin, J. Gao, Q. Guo, and Z. Zhang, "In situ formation of surface-induced oxygen vacancies in Co_9S_8/CoO/NC as a bifunctional electrocatalyst for improved oxygen and hydrogen evolution reactions," *Nanomaterials*, vol. 11, no. 9, article 2237, 2021.

[31] A. T. A. Ahmed, A. S. Ansari, S. M. Pawar, B. Shong, H. Kim, and H. Im, "Anti-corrosive FeO decorated $CuCo_2S_4$ as an efficient and durable electrocatalyst for hydrogen evolution reaction," *Applied Surface Science*, vol. 539, article 148229, 2021.

[32] T. Wang, L. Wu, X. Xu et al., "An efficient Co_3S_4/CoP hybrid catalyst for electrocatalytic hydrogen evolution," *Scientific Reports*, vol. 7, no. 1, article 11891, 2017.

[33] A. T. A. Ahmed, C. Ho Lee, A. Saad Ansari et al., "Hybridized heterostructure of CoS and MoS_2 nanoparticles for highly-efficient and robust bifunctional water electrolysis," *Applied Surface Science*, vol. 592, article 153196, 2022.

[34] A. T. A. Ahmed, A. S. Ansari, H. Kim, and H. Im, "Ion-exchange synthesis of microporous Co_3S_4 for enhanced electrochemical energy storage," *International Journal of Energy Research*, vol. 46, no. 4, pp. 5315–5329, 2022.

[35] A. T. A. Ahmed, H. S. Chavan, Y. Jo et al., "One-step facile route to copper cobalt sulfide electrodes for supercapacitors with high-rate long-cycle life performance," *Journal of Alloys and Compounds*, vol. 724, pp. 744–751, 2017.

[36] A. A. Ansari and S. D. Sartale, "The calculation of electronic parameters of Al/TiO_2/p-Si MOS structure formed using TiO2 thin films grown by thermal oxidation of sputtered Ti films," *Advanced Science Letters*, vol. 22, no. 4, pp. 1013–1016, 2016.

[37] L. Zhu, L. Liu, G. Huang, and Q. Zhao, "Hydrogen evolution over N-doped CoS_2 nanosheets enhanced by superaerophobicity and electronic modulation," *Applied Surface Science*, vol. 504, article 144490, 2020.

[38] A. T. A. Ahmed, S. Sekar, S. Lee, H. Im, V. Preethi, and A. S. Ansari, "Nitrogen-doped cobalt sulfide as an efficient electrocatalyst for hydrogen evolution reaction in alkaline and acidic media," *International Journal of Hydrogen Energy*, 2022.

[39] L. Givalou, M. Antoniadou, D. Perganti et al., "Electrodeposited cobalt-copper sulfide counter electrodes for highly efficient quantum dot sensitized solar cells," *Electrochimica Acta*, vol. 210, pp. 630–638, 2016.

[40] C. C. Gudal, U. N. Pan, D. R. Paudel, M. R. Kandel, N. H. Kim, and J. H. Lee, "Bifunctional P-intercalated and doped metallic (1T)-copper molybdenum sulfide ultrathin 2D-nanosheets with enlarged interlayers for efficient overall water splitting," *ACS Applied Material & Interfaces*, vol. 14, no. 12, pp. 14492–14503, 2022.

[41] A. A. Ansari and S. D. Sartale, "Effect of processing parameters on size, density and oxygen reduction reaction (ORR) activity of Pd nanoparticles grown by spin coating," *Surface and Coatings Technology*, vol. 281, pp. 68–75, 2015.

[42] S. Lee, G. Baek, J. H. Lee et al., "Molecular layer deposition of indicone and organic-inorganic hybrid thin films as flexible transparent conductor," *Applied Surface Science*, vol. 525, article 146383, 2020.

[43] Y. C. Wu, A. S. Ansari, D. Dutta et al., "Catalyzed decomposition of methanol-d4on vanadium nanoclusters supported on an ultrathin film of Al_2O_3/NiAl(100)," *The Journal of Physical Chemistry C*, vol. 126, no. 8, pp. 3903–3914, 2022.

[44] S. Choi, A. S. Ansari, H. J. Yun, H. Kim, B. Shong, and B. J. Choi, "Growth of Al-rich AlGaN thin films by purely thermal atomic layer deposition," *Journal of Alloys and Compounds*, vol. 854, article 157186, 2021.

[45] A. A. Ansari and S. D. Sartale, "Controlled growth of thermally stable uniform-sized Ag nanoparticles on flat support and their electrochemical activity," *Applied Physics A*, vol. 119, no. 2, pp. 503–516, 2015.

[46] J. W. Murray and J. G. Dillard, "The oxidation of cobalt(II) adsorbed on manganese dioxide," *Geochimica et Cosmochimica Acta*, vol. 43, no. 5, pp. 781–787, 1979.

[47] Y. Wang, Y. Nie, W. Ding et al., "Unification of catalytic oxygen reduction and hydrogen evolution reactions: highly dispersive Co nanoparticles encapsulated inside Co and nitrogen co-doped carbon," *Chemical Communications*, vol. 51, no. 43, pp. 8942–8945, 2015.

[48] M. Chauhan, K. P. Reddy, C. S. Gopinath, and S. Deka, "Copper cobalt sulfide nanosheets realizing a promising electrocatalytic oxygen evolution reaction," *ACS Catalysis.*, vol. 7, no. 9, pp. 5871–5879, 2017.

[49] J. B. Wu, Y. F. Lin, J. Wang et al., "Correlation between N 1s XPS binding energy and bond distance in metal amido, imido, and nitrido complexes," *Inorganic Chemistry*, vol. 42, no. 15, pp. 4516–4518, 2003.

[50] K. Chhetri, B. Dahal, T. Mukhiya et al., "Integrated hybrid of graphitic carbon-encapsulated Cu_xO on multilayered mesoporous carbon from copper MOFs and polyaniline for asymmetric supercapacitor and oxygen reduction reactions," *Carbon*, vol. 179, pp. 89–99, 2021.

[51] J. L. Gunjakar, B. Hou, A. I. Inamdar et al., "Two-dimensional layered hydroxide nanoporous nanohybrids pillared with zero- dimensional polyoxovanadate nanoclusters for

enhanced water oxidation catalysis," *Small*, vol. 14, no. 49, article 1703481, 2018.

[52] S. M. Pawar, B. S. Pawar, P. T. Babar et al., "Electrosynthesis of copper phosphide thin films for efficient water oxidation," *Materials Letters*, vol. 241, pp. 243–247, 2019.

[53] S. M. Pawar, B. S. Pawar, P. T. Babar et al., "Nanoporous $CuCo_2O_4$ nanosheets as a highly efficient bifunctional electrode for supercapacitors and water oxidation catalysis," *Applied Surface Science*, vol. 470, pp. 360–367, 2019.

[54] S. M. Ji, A. Muthurasu, K. Chhetri, and H. Y. Kim, "Metal-organic framework assisted vanadium oxide nanorods as efficient electrode materials for water oxidation," *Journal of Colloid and Interface Science*, vol. 618, pp. 475–482, 2022.

[55] M. R. Kandel, U. N. Pan, D. R. Paudel, P. P. Dhakal, N. H. Kim, and J. H. Lee, "Hybridized bimetallic phosphides of Ni-Mo, Co-Mo, and Co-Ni in a single ultrathin-3D-nanosheets for efficient HER and OER in alkaline media," *Composites Part B: Engineering*, vol. 239, article 109992, 2022.

[56] P. Babar, A. Lokhande, H. H. Shin et al., "Cobalt iron hydroxide as a precious metal-free bifunctional electrocatalyst for efficient overall water splitting," *Small*, vol. 14, no. 7, article 1702568, 2018.

[57] Y. Surendranath, M. W. Kanan, and D. G. Nocera, "Mechanistic studies of the oxygen evolution reaction by a cobalt-phosphate catalyst at neutral pH," *Journal of the American Chemical Society*, vol. 132, no. 46, pp. 16501–16509, 2010.

[58] A. Damjanovic, M. A. Genshaw, and J. O. M. Bockris, "The mechanism of oxygen reduction at platinum in alkaline solutions with special reference to H2O2," *Journal of The Electrochemical Society*, vol. 114, no. 11, p. 1107, 1967.

[59] L. Negahdar, F. Zeng, S. Palkovits, C. Broicher, and R. Palkovits, "Mechanistic aspects of the electrocatalytic oxygen evolution reaction over Ni–Co oxides," *Chem Electro Chem.*, vol. 6, no. 22, pp. 5588–5595, 2019.

[60] W. H. Lee, M. H. Han, Y. J. Ko, B. K. Min, K. H. Chae, and H. S. Oh, "Electrode reconstruction strategy for oxygen evolution reaction: maintaining Fe-CoOOH phase with intermediate-spin state during electrolysis," *Nature Communications*, vol. 13, no. 1, p. 605, 2022.

[61] K. Chhetri, A. Muthurasu, B. Dahal et al., "Engineering the abundant heterointerfaces of integrated bimetallic sulfide-coupled 2D MOF-derived mesoporous CoS_2 nanoarray hybrids for electrocatalytic water splitting," *Materials Today Nano*, vol. 17, article 100146, 2022.

[62] S. Shit, S. Chhetri, W. Jang et al., "Cobalt sulfide/nickel sulfide heterostructure directly grown on nickel foam: an efficient and durable electrocatalyst for overall water splitting application," *ACS Applied Materials & Interfaces*, vol. 10, no. 33, pp. 27712–27722, 2018.

[63] S. Tang, X. Wang, Y. Zhang, M. Courté, H. J. Fan, and D. Fichou, "Combining Co_3S_4 and Ni:Co_3S_4 nanowires as efficient catalysts for overall water splitting: an experimental and theoretical study," *Nanoscale*, vol. 11, no. 5, pp. 2202–2210, 2019.